HEPL-78

I

THE STRUCTURE OF THE PROTON

by

E. E. Chambers and R. Hofstadter

Technical Report No. HEPL-78

Contract No. AF 18(600)-646

Project No. R-357-20-9

April 1956

High-Energy Physics Laboratory

W. W. Hansen Laboratories of Physics

Stanford University

Stanford, California

500-1

DISCLAIMER

This report was prepared as an account of work sponsored by an agency of the United States Government. Neither the United States Government nor any agency Thereof, nor any of their employees, makes any warranty, express or implied, or assumes any legal liability or responsibility for the accuracy, completeness, or usefulness of any information, apparatus, product, or process disclosed, or represents that its use would not infringe privately owned rights. Reference herein to any specific commercial product, process, or service by trade name, trademark, manufacturer, or otherwise does not necessarily constitute or imply its endorsement, recommendation, or favoring by the United States Government or any agency thereof. The views and opinions of authors expressed herein do not necessarily state or reflect those of the United States Government or any agency thereof.

DISCLAIMER

Portions of this document may be illegible in electronic image products. Images are produced from the best available original document.

II

Bibliographical Control Sheet

1. Originatingagency and monitoring agency:

   O. A. : Stanford University, Stanford, California
   M. A. : Physics Division, Office of Scientific Research

2. Originating agency and monitoring agency report number:

   O. A. : Stanford Report No.: HEPL-78
   M. A. : Report Control No.: TN-56-151

3. Title and classification of title: THE STRUCTURE OF THE PROTON

4. Personal Author: E. E. Chambers and R. Hofstadter

5. Date of report: April 1956

6. Pages: 28

7. Illustrative material: 16

8. Prepared for Contract No.: AF 18(600)-646

9. Prepared for Project No.: R-357-20-9

10. Security classification: UNCLASSIFIED

11. Distribution limitations: None

12. Abstract: See next page

HEPL-78

The Structure of the Proton*

E. E. Chambers† and R. Hofstadter

Department of Physics and High-Energy Physics Laboratory
Stanford University, Stanford, California

ABSTRACT

The structure and size of the proton have been studied by means of the methods of high-energy electron scattering. The elastic scattering of electrons from protons in polyethylene has been investigated at the following energies in the laboratory system: 200, 300, 400, 500, 550 Mev. The range of laboratory angles examined has been 30° to 135°. At the largest angles and the highest energy, the cross section for scattering shows a deviation below that expected from a point proton by a factor of about nine. The magnitude and variation with angle of the deviations determine a structure factor for the proton, and thereby determine the size and shape of the charge and magnetic-moment distributions within the proton. An interpretation, consistent at all energies and angles and agreeing with earlier results from this laboratory, fixes the rms radius at $0.77 \pm 0.10 \times 10^{-13}$cm for each of the charge and moment distributions. The shape of the density function is not far from a Gaussian with rms radius 0.70×10^{-13}cm or an exponential with rms radius 0.80×10^{-13}cm. An equivalent interpretation of the experiments would ascribe the apparent size to a breakdown of the Coulomb law and the conventional theory of electromagnetism.

500-3

I. INTRODUCTION

Some time ago deviations from point-charge scattering of electrons against the proton were demonstrated at laboratory energies of 188 Mev and 230 Mev and at laboratory angles between 90° and 140°.[1,2] In those investigations, the cross section varied over approximately a factor of 200 between the forward and backward angles. Yet the deviation of the experimental data from a point-charge-point-moment curve was something less than a factor of two at the largest angles, and the experimental error amounted to perhaps a fourth of the deviation. It was not possible to determine accurately the relative separate proportions of charge structure and moment structure which could give agreement with experiment. However, it was shown that equal form factors for charge and moment agreed excellently with the experimental data and the size was fixed at 0.74×10^{-13}cm $\pm$ 0.24×10^{-13}cm for the rms radius of the charge and moment distributions. Since the reduced de Broglie wavelength of the probing electrons was larger than the "size" of the protonic distributions, it was not possible to distinguish between different shapes for the density distributions of the charge cloud and moment cloud.

Recently we have completed the construction of a larger analyzing spectrometer for the scattered electrons. This spectrometer can bend and analyze electrons with energies up to 550 Mev. At this energy the reduced de Broglie wavelength approaches one-half the size of the proton determined by the earlier experiments, and the experimental angular distribution

is no longer insensitive to the shape of the mesonic clouds in the proton. We have taken advantage of the shape sensitivity and have attempted to find a model of the proton which fits not only the angular distribution at the highest energies, but also those at lower energies where only a size is determined. These matters will be treated in detail below.

II. EXPERIMENTAL METHOD

In many respects the experimental apparatus and method are similar to those reported in earlier papers.[3,4,5] The new features relate to a larger spectrometer and its accessories in the new installation in the "end station" of the Stanford linear accelerator. The end station and bunker area (beam-switching taking place in the latter) will not be described in this paper since they have already been discussed previously.[6] The details of the linear accelerator are also discussed in the reference above.

Fig. 1 shows the experimental arrangement used in the electron-scattering experiments in the end station. The electron beam is deflected and dispersed by the first magnet and passes through the energy-defining slit. After passing through the second magnet, the beam is returned parallel to its original direction and refocused at the target. The beam travels in vacuum from accelerator through the magnets, through a secondary electron monitor, and through a thin window (3-mil aluminum) into air before it strikes the target foil. The secondary monitor is of a type we have used previously [7] and is equivalent

to a thickness of 5 mils of aluminum. The monitor and thin exit window are at a mean distance of eight inches from the target and so a typical widening at 400 Mev of the focused spot, because of the multiple scattering in monitor and window, amounts to only one millimeter. The additional divergence of the beam is also not large and amounts to $\pm 1^{\circ}$. For the angular structure involved in these experiments, this spread is entirely negligible. The angular spread in the original beam, before striking the monitor and the exit window, is less than 0.2°. In future experiments the secondary monitor will be replaced by the large Faraday cup, shown dotted in the figure, which is now nearing completion.

The target holder is built in the form of a ladder with the open spaces serving to hold the target specimens. A typical target layer is four inches wide and one and one-half inches high. In the case of polyethylene, a typical target thickness is 170 mils. Thus, the uncertainty in angle is determined principally by the target itself and not by the monitor or exit window. The target holder is controllable by remote means and can be moved up or down to bring different targets into the beam or can be rotated and set anywhere within 360°. Ten different targets can be placed in the target holder for a given run. A bell jar can be set over the target assembly when vacuum conditions are required. Thus far the bell jar has not been used.

From the target foil the scattered beam travels through five inches of air, through a thin entrance window (3 mils

of aluminum) and then in between the jaws of a lead slit which defines the entrance aperture of the magnetic spectrometer. The target-to-slit distance is usually 26 inches. The pole face of the spectrometer lies at a distance 10.0 inches beyond the lead entrance-slit. The scattered electrons arriving at the magnet are then bent through 180° and double-focused by the magnetic spectrometer. The spectrometer and its mounting will not be described.

The heart of the apparatus is the 180° double-focusing magnetic spectrometer sketched in Fig. 2. The instrument is basically a 30-ton analyzing magnet of a design similar to the smaller 2-1/2 ton magnet used in previous electron-scattering studies.[3] The latter instrument is, in turn, quite similar to the spectrometer of Snyder et al[8] which, itself, is a modification of the original idea of Siegbahn and Svartholm.[9] The presently described spectrometer has been newly designed and is not a scaled-up version of a previous magnet. The radius of curvature of the central trajectory in this magnet is 36 inches and the maximum field obtained on this radius is approximately 20,000 gauss, although the magnet has not often been used in experiments at this maximum field.

As is well known, the purpose of the magnet is to collect scattered electrons from a small area on a target foil, analyze their energy distribution, and focus them upon a small detector after they have passed through the exit-defining slit of the spectrometer. The maximum useful aperture of this spectrometer is approximately 1/1000 of the entire

solid angle, and the dispersion of the instrument is such that electrons, which differ in energy by 1%, are focused near the central trajectory to separate spots 1.33 inches apart. An important feature of the magnet is that electrons originating from a point on the target are "double-focused" or imaged as a point on the detector. Naturally the image is not perfect and small aberrations or distortions are present as in many optical systems.

In actual practice, electrons with energies up to 510 Mev have been analyzed and studied in these experiments. These correspond to electrons of incident energy >50 Mev in the laboratory, scattered at 30° by protons. Electron trajectories can, in principle, fill an area of 15 × 3 inches; these dimensions refer to the pole width and pole gap, respectively. At the present time, a bronze vacuum chamber within the magnet reduces the internal dimensions available to electrons to a cross-sectional area of 14 × 2 inches. Three radial holes, 4 inches in diameter, pass through the outer yoke of the magnet and communicate with three similar, but smaller, holes in the bronze chamber. Into these holes we have inserted radial magnetic probes to study the field distribution in the median plane of the magnet. These holes lie at the 30°, 90°, 120° azimuths around the magnet circle. The magnetic fields at the 30° and 120° ports have been observed to be 2% smaller than those in the middle of the magnet, at the 90° port. A typical magnetic profile is shown in Fig. 3. Up to 14,000

gauss the field-current curve is essentially linear, and the magnet is unsaturated; 14,000 gauss corresponds to approximately 400 Mev.

Double focusing is achieved by tapering the pole faces so that the field falls off at larger radii in a manner similar to the field in a betatron. The field is required to fall off according to the inverse square root of the radius in this type of instrument. This means that

$$\frac{dH}{H} = -\frac{1}{2}\frac{dr}{r} \qquad (1)$$

where H and r refer to the field and the value of the radius on or near the central trajectory in the median plane. Expecting that the field in the gap would fall off as the reciprocal of the gap itself, or in other words,

$$\frac{dH}{H} = -\frac{dy}{y} = -\frac{1}{2}\frac{dr}{r} \qquad (2)$$

where y is the pole gap at any radius, the pole faces were given a linear taper corresponding to Eq. (2). At the edges of the pole, a lip was machined into the steel to prevent a too-rapid decline to zero. The linear taper has proved satisfactory as shown by the radial measurements of the field. The measurements show that up to 400 Mev, relation (1) is well satisfied between radii 33.5 and 38.5 inches. At higher fields this region contracts until at 550 Mev it is only approximately two inches wide. Consequently, up to 400 Mev, the field is as it should be for double focusing. Photographs and visual observation of the exit spot show that focusing does indeed take place in two dimensions, as expected.

A small fringing field exists at the entrance and exit of the spectrometer. The effect of this fringing field is such as to increase the effective magnetic path along the central trajectory by about 2%. This increase in path has no important effect on any of the measurements or uses of the spectrometer.

Some essential statistics regarding the magnet may prove useful to others.[10] As shown in Fig. 2, the magnet is built in two symmetrical-forged halves, each weighing approximately 15 tons, and having the gross shape of a capital D. Perpendicular to the D plane, the thickness of the iron in each half is 21.75 inches. The outer radius of the D is 57 inches, making the total height of the magnet 9.60 feet. When the two halves are assembled and the magnet is viewed from the input end, an H-like space around the pole gap may be seen accommodating the electrical coils and the bronze vacuum chamber. The coils are constructed of 0.467-inch-square copper tubing, having a round hole of 0.275-inch-diameter, and are watercooled.[11] There are 256 turns around the poles and the coils are wound four at a time in two bundles to make eight turns per pancake layer. In this way adequate cooling can be provided. All the turns are electrically in series but there are 64 parallel water circuits. The nominal capacity of the magnet is 800 amperes at 250 volts, although as much as 1000 amperes have been put through it. At 800 amperes the coils are barely warm; 400 amperes

correspond approximately to 400 Mev on the linear part of the magnet characteristic. The outer return yoke is 11.75 inches thick on each side and 8.5 inches thick radially. The inner return is a half-cylinder 21.75 inches thick and 47 inches in diameter. Each half of the magnet is equipped with a single large handling lug. A fourth hold through the outer return yoke and vacuum chamber permits an x-ray beam to pass through the magnet when desired, the magnetic field itself being used as a clearing field.

Because of the poor duty cycle of the linear accelerator, a heavy shield must guard the detector from background radiation. In this installation a ten-ton shield constructed of heavy concrete on the outside, lead on the inside, surrounds the Cerenkov detector. The shield is carried on the magnet by means of a massive platform overhanging the target assembly as shown in Fig. 1. As the magnet rotates the platform and shield are carried with it. The magnet, platform, and shield can also be moved radially to and from the target on two large ways. Within the ways are many cylindrical rollers which take the weight of the 40-odd tons of the spectrometer. The ways are fastened to a modified double five-inch anti-aircraft obsolete gun mount kindly furnished by the Bureau of Ordnance, U. S. Navy, at the request of the Office of Naval Research.[12] The modifications, which transformed the mount from a military device to a scientific instrument, were carried out at the San Francisco Naval Shipyard.[13] The whole gun mount and its assembly can be

accurately moved by remote control about the target center. Repeated trials positioning the assembly appear to agree within better than 0.05 degree.

The Cerenkov detector is a truncated lucite cone with a 2.75-inch-diameter input face and a four-inch-diameter termination which couples onto a Dumont 5-inch photomultiplier. The Cerenkov counter is seated behind lead slit jaws which determine the transverse width seen by the detector at the target. Usually a 1.75-inch slit is used to determine the effective target width and the energy slit is, of course, variable but accommodates up to a spread of about 1.3% in energy (momentum, to be perfectly accurate). The response of the Cerenkov detector is tested before each run and always shows a wide plateau (30 to 40 volts wide) for electrons ranging from less than 200 Mev to the maximum studied (510 Mev). The distribution of Cerenkov counter pulses is checked with a twenty-channel discriminator before each run and has shown insignificant differences at any energy studied: a narrow peak is observed at all energies.

As is usual in these experiments, the incident electron beam is viewed on a crystal plate of CsBr(Tl) through a telescope. After centering the spot and minimizing the spot size, the crystal is withdrawn and the target is inserted. Periodic checks are made to see that the spot remains the same during an experiment. The spot has varied between a width of 0.25 and 0.50 inch in the course of these experiments.

The height of the spot has always been less than 0.25 inch and more usually about 0.13 inch. Unfortunately, the main part of the beam can move around within the width of the spot itself and can sometimes even divide into two parts. This has the annoying effect of varying the incident energy by perhaps as much as 1/2%. Usually a 1% energy band has been employed in these experiments. Consequently, the scattered electrons may show an energy variation of something approaching 1/2% during a particular run. The elastic profiles may, therefore, shift during a run, and points on the steep sides of these curves will then not reproduce exactly. We believe that this is the main cause of the 5 to 10% fluctuations that we observe when trying to reproduce data from night to night and perhaps even during a single night's run. However, the latter fluctuations are more likely 5% at the worst.

Although most runs have been taken with polyethylene targets, a few points which check the polyethylene data have been taken with a gas target.[14] In this case the gas target previously described has been used[2], although its length has been increased to eight inches to allow better observations at small and large angles.

III. RESULTS

The shape and characteristics of an elastic profile taken at 60° at 400 Mev incident energy are shown in Fig. 4. This curve was taken with statistics about four times as

numerous as those usually employed in a run in order to determine the characteristic appearance of the profile. Similar curves taken at larger and smaller angles have the same appearance within our experimental errors. Consequently, relatively little error will be obtained by employing the same method at all angles in correcting for the area between AB and CE which corresponds to the bremsstrahlung tail of the elastic peak. Our method has been to continue the straight line AC into the carbon background and calculate the area under the roughly trapezoidal peak. Different and independent methods have been used consistently by each of the two authors to estimate the peak areas, but the results obtained always haveagreed within better than the experimental errors. It is to be understood, of course, that the polyethylene-carbon difference is used in obtaining the area under the proton peaks. Excellent agreement is found between such differences and estimations of the areas of the proton peaks obtained by sketching in the relatively flat (or slightly upturned towards lower energies) background in polyethylene alone, on top of which the proton peak "rides."

In finding the area under the proton peak, the half-width of the curve is always expressed in energy units. The conversion from potentiometer readings (magnet current) to an energy scale has been accomplished by (1) using a magnetic probe to find the field in the magnet and assuming the energy is proportional to the field and (2) using the positions of the centers of the proton peaks and relativistic

kinematics to determine the energy of the scattered electrons at any given incident energy and at any given angle. The typical appearance of such a theoretical curve is shown in Fig. 5. Methods (1) and (2) have been combined to give the most consistent calibration curve, using the calibration curve of the deflecting magnet (Fig. 1) to find the incident energy. The two methods agreed so well from the first comparison that it was hardly necessary to make any changes. However, the methods have been merged in a self-consistent way to give what we think is the most accurate final calibration curve. As stated before, this curve tells us that the magnet is essentially linear (energy vs magnet current) up to about 400 Mev, which corresponds to 204 units on the potentiometer scale. In almost every measurement we have made, the proton peak has been below 204 on the potentiometer to avoid saturation and possible defocusing problems. However, in operating at the highest energies and smallest angles, we have occasionally overstepped the 204 limit, but in no way that we believe has caused any serious trouble. Of course, in these cases, as well as in all others, we used the calibration scale to determine the energy width of all peaks. It is not believed that any error larger than 5% can be introduced even at the highest energies and smallest angles. Explicitly, the only cases in which the 204 boundary was passed were at 500 Mev, 45°, and 550 Mev, at angles less than 60°.

Photographic registration of the focused spots at the output of the spectrometer show that the dispersion obtained

experimentally is very close to that calculated with Judd's formula.[15] This is further assurance that the calculation of energy width from magnet current is correct. In this connection it should be pointed out that the areas under the proton peaks still need a correction for the constant width of the upper spectrometer slit. The constant slit value was set at 1.3%, which means that, at all momenta, 1.3% intervals are selected for passage into the detector. Thus, at smaller energies of the scattered electrons (larger angles--see Fig. 5), the slit assumes a smaller absolute energy width. This correction varies as the reciprocal of the energy so that at smaller energies the area has been increased by 1/E relative to the higher energies. This is the usual correction made in beta-ray spectrographs.

Other small corrections have been made for radiation straggling in the targets and for the radiative calculation of Schwinger. Thickness normalizations have been made where the target thickness varied from angle to angle, because of a half-angle setting as is customary in scattering experiments, or in the case of the gas target. In some experiments the target angle was not varied, although most of the time it was. Consistent results were always obtained.

Thick target effects were investigated with some care. However, they appear to be absent or at any rate are so small that they do not lie consistently outside our experimental errors. Aside from the normalization due to source thickness, the totals of all corrections to the data were never larger

than 10% and were usually considerably smaller. By this we mean, of course, relative corrections between the smallest and largest angles. The Schwinger correction itself is approximately a 20% correction in the absolute cross section. So far we have confined our attention to relative cross sections exclusively.

We have obtained rough absolute cross sections only by knowing the absolute response of the secondary emitting monitor.[7] We shall return to this point after discussing the relative cross sections and the angular distributions which do not require absolute measurements. Thus, in the ensuing material, except where noted, we shall be speaking of relative cross sections only.

By measuring areas under the proton peaks at various angles at a given incident energy, we may prepare relative angular distribtuions. Such angular distributions are shown in Figs. 6, 7, 8 and 9. The experimental points are the black dots attached to the bars indicating the limits of experimental error, usually not statistical, but primarily due to the type of fluctuation we have mentioned earlier. The data represent in each case the results of at least two separate runs except at 300 Mev, where only a single run was taken. We have also made a run at 200 Mev, but since it agrees excellently with the earlier data taken with the smaller spectrometer,[1,2] we do not show it separately here. The 200-Mev data appear in Figs. 11 and 13, along with data of all other energies. In Figs. 6--9 there also appear solid

lines going through most of the experimental curves. These are not experimental lines, but are actually the result of theoretical calculation which we shall discuss shortly. Also shown in Figs. 6--9 are the point-charge curves of Rosenbluth.[16] These are designated $r_e = 0$, $r_m = 0$, to indicate that the rms radius of the charge and magnetic-moment distributions are each zero, in other words, that the charge and moment are points.

In order to compare the experimental curves with theory, we have employed the same phenomenological scheme presented in the earlier paper.[2] This amounts to using a separate form factor F_1 for charge and Dirac moment of the proton, and F_2, an additional independent form factor for the anomalous or Pauli magnetic moment. In the static limit, $F_1 = F_2 = 1$ and the Pauli moment takes on its value, 1.79 nuclear magnetons, compared with the Dirac value, 1.0 nuclear magneton. $F_1 \neq 1$ implies a spread-out charge and spread-out Dirac moment and $F_2 \neq 1$ implies a spread-out Pauli moment. For reference, the Rosenbluth formula with phenomenological form factors is given in Eq. (3).

$$\sigma = \frac{e^4}{4E^2}\left(\frac{\cos^2\frac{\theta}{2}}{\sin^4\frac{\theta}{2}}\right)\frac{1}{1+\frac{2E}{M}\sin^2\frac{\theta}{2}}\left\{1+\frac{q^2}{4M^2}\left[2\,(F_1+\mu F_2)^2\tan^2\frac{\theta}{2}+\mu^2F_2^2\right]\right\}. \quad (3a)$$

where

$$q = \frac{\frac{2}{\lambda\!\!\!^{-}}\sin\frac{\theta}{2}}{\sqrt{1+\frac{2E}{M}\sin^2\frac{\theta}{2}}} \quad \ldots\ldots\ldots\ldots\ldots\ldots\ldots\ldots (3b)$$

and $\lambda\!\!\!^{-}$ is the de Broglie wavelength of the electron.

The effect of using the form factors is shown in Fig. 10. For this figure an exponential model of the proton is assumed as an example. By this, it is meant that the proton has a charge density given by

$$\rho_{\text{Expon}} = \rho_0 e^{-r} \tag{4}$$

In Eq. (4), as well as in subsequent ones, we shall omit the parameter corresponding to an rms size, although, of course, the exponential has to be expressed in dimensionless units. For example, ρ_{Expon} can be expressed as $\rho_0 \exp(-r/a)$ where 3.48a is the rms radius. The assumption that the magnetic-moment distribution has a shape and size equal to that of the charge distribution means that the magnetic-moment density has a distribution of exponential type with the same radius as the charge and points in a single direction everywhere throughout the proton. Under these conditions its form factor will be exactly like that of the charge distribution. The actual computation of explicit form factors has been carried out, for example, by Rose,[17] Smith,[18] Schiff,[19] and others. We shall not reproduce here any of the resultant expressions obtained by integration of the appropriate Born-approximation integral. It is known that the Born approximation is accurate for the proton to better than a few tenths of 1%.[20]

The features of all other calculations, with different proton models, are similar to those shown in Fig. 10. The general effect is to reduce the scattering below that due to a point charge. At small angles the form factors approach

unity and all curves meet with the point-charge curve. Thus, relative fitting of the experimental points to the theoretical curves benefits from the joining-up that must occur at small angles.

When both the shape and size of the protonic model are assumed to be the same, Eq. (3) shows that the square of the form factor may be factored out and the result is a point-charge curve multiplied by the square of a form factor. Such calculations are the easiest to make.

With the models above described, the following shapes have been examined:

$$\rho_a = \rho_1 e^{-r^2} \qquad \text{"Gaussian"} \tag{5}$$

$$\rho_b = \rho_2 (e^{-r}/r^2) \qquad \text{Yukawa}_1 \tag{6}$$

$$\rho_c = \rho_3 (e^{-r}/r) \qquad \text{Yukawa}_2 \tag{7}$$

$$\rho_d = \rho_4 r e^{-r} \tag{8}$$

$$\rho_e = \rho_5 r^2 e^{-r} \tag{9}$$

$$\rho_f = \rho_6 r^2 e^{-r^2} \tag{10}$$

in addition to the exponential model of Eq. (4) and the uniform and shell distributions. These models cover a very wide range, and almost any reasonable shape can be approximated by one of them. The best fits are obtained with models 4, 5, 8 and 9. None of the other models can be made to fit the data at all energies. Each model naturally requires a slightly different rms radius for the best fit, but all successful models give a radius very close to 0.75×10^{-13}cm. Henceforth, we shall use the Fermi unit = 10^{-13}cm and shall express all lengths in these units.

For the exponential proton, which we shall take as a typical successful model, the best fit is obtained with the rms radii, $r_e = 0.8$ and $r_m = 0.8$ fermi. Figs. 6 through 9 show the quality of the fit at various energies. A summary of all the data taken together can be well presented by plotting the square of the common form factor vs q^2 where q is given in Eqs. (3). Such a plot is given in Fig. 11. Since F^2 is a function of q^2, a single theoretical curve suffices for all energies. This is not the case when the charge and moment radii are unequal, for then a separate theoretical curve must be prepared for each energy. Fig. 11 shows that the exponential model with radii equal to 0.8 fermi is very good at all energies. As an example of the tolerance of the exponential fit, Fig. 12 shows the exponential model with equal radii of 0.6 fermi. This is a case where a good model with an "incorrect" size will not fit. On the other

hand, the Gaussian model with rms radii equal to 0.7 fermi will fit just as well as the exponential model with 0.8 fermi. Fig. 13 shows how well this model fits. The theoretical plot in this case is a straight line. The Yukawa model (6) with equal radii cannot be made to fit even with radii as large as 1.5 fermi.

The case of two unequal sizes has also been investigated. It has not been possible to find a unique model with two unequal sizes for the charge and moment clouds that will fit the data at all energies (within, of course, the tolerance permitted by experiment). A model with a small magnetic distribution cannot be made to fit under any circumstances. Fig. 14 shows a typical case for $r_e = 0.8$ and $r_m = 0.4$. It is possible to find suitable fits by using a larger magnetic-moment size and a smaller charge size. For example, it might be possible to choose $r_e = 0.6$ and $r_m = 0.9$, and the data at all energies would be satisfied but not quite so well as with the models having equal sizes. On the other hand, a point-charge and spread-out moment will not fit, as shown by the summary graph given in Fig. 15. The results are similar for other models, such as the exponential and uniform. The limit on minimum charge size allowed by these experiments appears to be about 0.6 fermi. The maximum is about 1.5 fermi. Similar figures apply to the magnetic moment radii.

The fitting above has been carried out entirely in a relative manner. In other words, each set of data at a given energy was multiplied by a constant factor to obtain the best fit with theory. The data at each energy were thus

treated independently. As stated above, the best fit converged on the models 4, 5, 8 and 9 with equal radii. A tabulation of the results is given in Table I.

It is also possible to correlate the data taken at one energy with the data taken at another energy. For example, if a 30° point at 300 Mev can be taken at the same time and under the same conditions as a 75° point at 550 Mev, the lower energy point can be used to normalize the data. The low energy point has an F^2 value that is essentially unity and thus, except for the Schwinger correction, the cross section can be obtained absolutely from the Rosenbluth point-charge curve. Now the Schwinger correction varies only by 3% between the two extremes under comparison and can be allowed for with great confidence since the whole effect itself is small. Consequently, the cross section at the larger angle can also be obtained in an absolute way. The absolute cross section at high q values (large-angle, high-energy) is very sensitive to shape and can distinguish between the different models proposed. Table II, below, gives a comparison among the predictions of the different models.

From the comparison it appears that model 8 fits the best although there is not much to choose between this model and the others. The table shows conclusively, however, that the small-charge cloud and large-moment cloud (Column 4) give an unacceptable fit to the data. It may be noticed that the experimental values appear to be a little high. This is probably a result of not knowing the absolute experimental

TABLE I

Model No.	Shape	RMS radius for best fit ($r_e = r_m$) in fermi units
4	e^{-r}	0.80 ± 0.05
5	e^{-r^2}	0.72 ± 0.05
8	re^{-r}	0.78 ± 0.05
9	r^2e^{-r}	0.75 ± 0.05
		0.77 ± 0.10
		Mean (best fit)

Table I.--This table gives a summary of the models and their values of rms radii which give the best fits. Equal radii for charge and moment are assumed.

TABLE II

Ratio	1 Experimental Ratio	2 Model 4 $r = 0.80$	3 Model 5 $r = 0.72$	4 Model 5 $r_e = 0$ $r_m = 1.0$	5 Model 8 $r = 0.80$	6 Model 8 $r = 0.77$	7 Model 9 $r = 0.75$
$\frac{\sigma\,(300\text{ Mev}, 30^\circ)}{\sigma\,(550\text{ Mev}, 75^\circ)}$	$440 \pm 10\%$	381	367	176	425	390	380
$\frac{\sigma\,(300\text{ Mev}, 30^\circ)}{\sigma\,(550\text{ Mev}, 60^\circ)}$	$164 \pm 10\%$	128	120	64.8	137	126	124
$\frac{\sigma\,(300\text{ Mev}, 60^\circ)}{\sigma\,(550\text{ Mev}, 75^\circ)}$	$18.9 \pm 10\%$	17.2	17.4	9.85	19.2	18.1	17.8
$\frac{\sigma\,(300\text{ Mev}, 60^\circ)}{\sigma\,(550\text{ Mev}, 60^\circ)}$	$6.96 \pm 10\%$	5.80	5.72	3.62	6.15	5.85	5.81

Table II.--This table shows the experimental ratios (Column 1) at the quoted energies and angles and lists in Columns (2--7) the predicted ratios for the various models represented therein. Where a single radius is given, the value applies to charge and moment. In Column 4 the charge radius is zero (a point) and the moment radius is 1.0 fermi.

energies precisely.

One of the authors has made an "absolute" determination of cross sections using the absolute efficiency of the secondary-electron monitor[7] and Judd's[15] calculations of effective solid angle of the spectrometer. These determinations agree excellently with the conclusions of the relative fitting procedure and also with the semi-absolute comparison of large-angle, high-energy and small-angle, low-energy data. The two authors have, therefore, independently confirmed the best choices for the charge and moment distributions within the proton.

In Fig. 16 we have displayed the result of these determinations. The ordinate of that figure is $4\pi r^2\rho$, which is a quantity proportional to the amount of charge in a shell at radius r. Three models (4, 5, and 8) are shown. All are good fits to the data at all energies and angles. Of the three, the model 8, the "hollow" exponential, is probably the best. Values of r_e are also given, which represent the best estimate of the rms radius of the charge distribution. The best value for r_m, the rms radius of the magnetic-moment distribution, is equal to r_e. The figure shows that a region is defined which outlines the three best fits and this region in the graph is what the experiments really determine. Any charge distribution lying in this region will define an equally good fit to the data. The region near radius zero is most poorly defined of all because the smallest amount of charge resides there due to the r^2 factor. In other words,

the exponential model, which has a high density at radius zero, cannot be well distinguished from a hollow exponential model in which the charge density is zero at radius zero, for just the reason given above. The fact that the hollow exponential model appears to be a slightly better fit than the exponential or Gaussian may suggest that the density drops a little, or flattens off, as radius zero is approached from larger values. At the moment this remark is rather speculative, but there is no reason why an improvement in the accuracy of the data cannot fix the behavior near zero. In any case, the disagreement with models of type 6 (Yukawa, shown in Fig. 16) and 7, which have large central cores, implies that the center of the proton does not have a dense charged core. Further improvement in accuracy will also help to clear up this point.

IV. DISCUSSION OF THE RESULTS

We have mentioned in this paper and in the earlier ones[1,2] that the analysis of our results is phenomenological. The analysis determines a charge distribution. From the charge distribution, an electrostatic potential can be calculated, using Poisson's equation in the usual way. Now this potential as a function of radius is the essential meat that can be extracted from the experiments. The basic integral of the Born aporoximation, containing, in its integrand, the potential multiplied by the product of ingoing and outgoing plane waves, underlies this fact. Consequently, electrostatic and magneto-

static potentials are the end products of these experiments.

One may ultimately determine a protonic model in the terms of a meson theory fitting the potentials we have found. These potentials have the feature that they flatten off as radius zero is approached, rather than increasing to infinity as the point-charge Coulomb law would predict. The effective deviations from the Coulomb law due to the flattening-off should then be the goals of a meson theory which will then give results consistent with the experimental data. Of course, here we see immediately that the simple assumption, that the Coulomb law breaks down (or equivalently, that Maxwell's equations do not hold) at small dimensions (less than 10^{-13}cm), will automatically explain our results and perhaps some other results.[21] This is what we have tried to point out in earlier papers,[1,2] but we have no direct evidence that this breakdown does take place. Phenomenologically the finite-size interpretation and the breakdown of the Coulomb law cannot be distinguished from each other by these experiments. Electron-electron scattering experiments at multibillion-electron-volts energy could do this. Since we cannot distinguish between these two possibilities, we have talked, for convenience, in terms of the finite-size interpretation. In any case, many of the implications of the two approaches are identical.

A satisfactory meson-theoretic approach to the quantitative explanation of the finite proton size is not yet

available, although Rosenbluth[16] has sketched how this may be done. In the absence of such a theory a naive approach would involve assuming that the proton is an undissociated Dirac particle a fraction f of the time and a spread-out meson cloud for the fraction (1 - f) of the time. During the latter time, scattering by the overturned value of the magnetic moment of the neutron, into which the proton was changed by emitting the π^+ meson, would take place and appropriate form factors allowing for times f and 1 - f would have to be employed in the computation. Such calculations are obviously not simple and will depend on the assumptions implicit in the particular meson theory to be used. We shall not consider such an interpretation at this time. However, it may be noted that the simple phenomenological interpretation given in this paper corresponds to a permanently dissociated proton. It is already clear from the experiments that a small dissociation time, corresponding to say, f = 0.9, will not suffice to fit the experimental facts, because in this case the scattering would be quite close to point-charge scattering.

By comparing cross sections at two energies at the same value of q, the ratio F_1/F_2 can be determined from Eq. (3a). This ratio will be independent of any assumed proton model. The comparison was made between three pairs of energies at a q^2 of about $4 \times 10^{26} cm^{-2}$ and a value for the ratio was obtained $F_1/F_2 = 1.1 \pm 0.2$.

ACKNOWLEDGMENT

We wish to thank Drs. D. R. Yennie, D. G. Ravenhall, F. Bloch, W. E. Lamb, Jr., J. A. McIntyre, and L. I. Schiff for many interesting discussions. Mr. H. Fried provided some calculations which simplified considerably our computational work, and we are very grateful for his help. Mr. Lance Rogers' help was invaluable in designing the magnetic spectrometer. We greatly appreciate the cooperation of the accelerator operating group for providing essentially continuous machine operation. We acknowledge, with many thanks, the work of a great many individuals, too numerous to mention explicitly, who have helped to obtain, construct and install the magnetic spectrometer and associated equipment.

REFERENCES

*The research reported here was supported jointly by the Office of Naval Research and the U. S. Atomic Energy Commission, and by the U. S. Air Force, through the Office of Scientific Research of the Air Research and Development Command.

†Lieutenant, United States Coast Guard. (Statements contained herein are private opinions and assertions of the authors and do not necessarily reflect the views of the Coast Guard.)

[1] R. Hofstadter and R. W. McAllister, Phys. Rev. 98, 217 (1955).

[2] R. W. McAllister and R. Hofstadter, Phys. Rev., in press.

[3] Hofstadter, Fechter, McIntyre, Phys. Rev. 92, 978 (1953).

[4] Hofstadter, Hahn, Knudsen, McIntyre, Phys. Rev. 95, 512 (1954).

[5] J. H. Fregeau and R. Hofstadter, Phys. Rev. 99, 1503 (1955).

[6] Chodorow, Ginzton, Hansen, Kyhl, Neal, Panofsky and Staff, Rev. Sci. Instr. 26, 134 (1955). See particularly Fig. 6.1 of this paper. See also W. K. H. Panofsky and J. A. McIntyre, Rev. Sci. Instr. 25, 287 (1954).

[7] G. W. Tautfest and H. R. Fechter, Rev. Sci. Instr. 26, 229 (1955).

REFERENCES (Continued)

[8]Snyder, Rubin, Fowler and Lauritsen, Rev. Sci. Instr. 21, 852 (1950).

[9]K. Siegbahn and N. Svartholm, Arkiv F. Math. Astron. Fysik 33A, No. 21 (1946); N. Svartholm, 33A, No. 24 (1946).

[10]The magnetic spectrometer was designed by L. Rogers and R. Hofstadter. The magnet was constructed by the Bethlehem Steel Corporation at Bethlehem, Pennsylvania. The authors are indebted to Messrs. Erb Gurney and W. Koegler for their invaluable assistance in designing and fabricating the forgings.

[11]The coils were wound and installed by the Pacific Electric Motor Co. of Oakland, California. Mr. James Allen of this organization worked out the coil design and we owe him our very best thanks.

[12]The loan of the gun mount is greatly appreciated. We wish to thank Lt. Malcolm Jones and Dr. W. E. Wright for their part in securing for us the use of the gun mount.

[13]Mr. Bernard Smith and his associates at the San Francisco Naval Shipyard carried out a most capable, thorough design and construction of this modification and we wish to express to them our heartiest thanks.

[14]We wish to thank Mr. R. Blankenbecler for taking the check-data.

[15]D. L. Judd, Rev. Sci. Instr. 21, 213 (1950). We wish to thank Dr. J. A. McIntyre and Mr. B. Chambers for taking the

REFERENCES (Continued)

spot photographs.

[16] M. N. Rosenbluth, Phys. Rev. 79, 615 (1950).

[17] M. E. Rose, Phys. Rev. 73, 279 (1948).

[18] J. H. Smith, Ph. D. Thesis, Cornell University, (1951); Phys. Rev. 95, 271 (1954).

[19] L. I. Schiff, Phys. Rev. 92, 988 (1953).

[20] H. Feshbach, Phys. Rev. 88, 295 (1952).

[21] D. R. Yennie and M. Lévy, to be published.

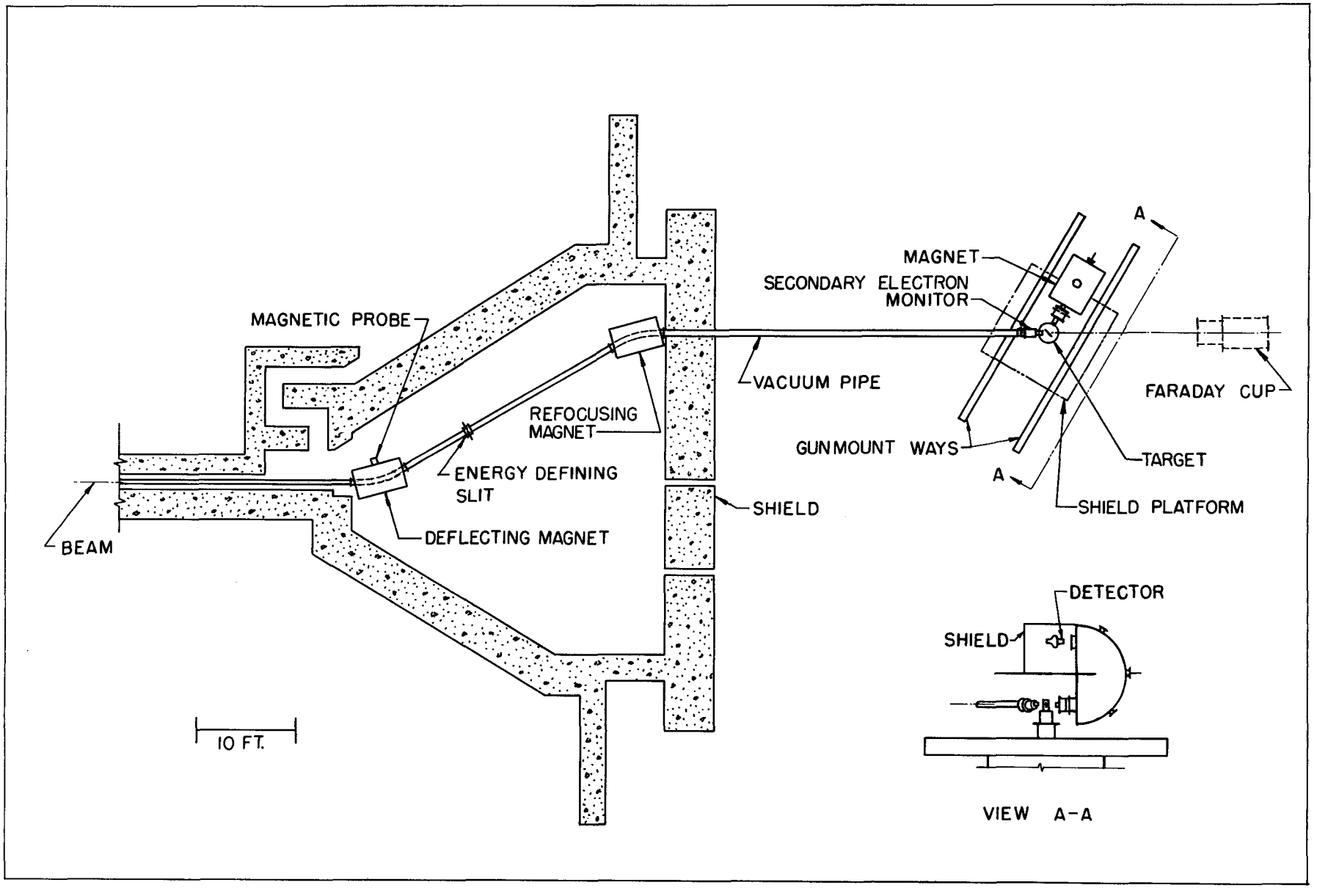

FIG. 1.——The installation of the magnetic spectrometer and scattering apparatus.

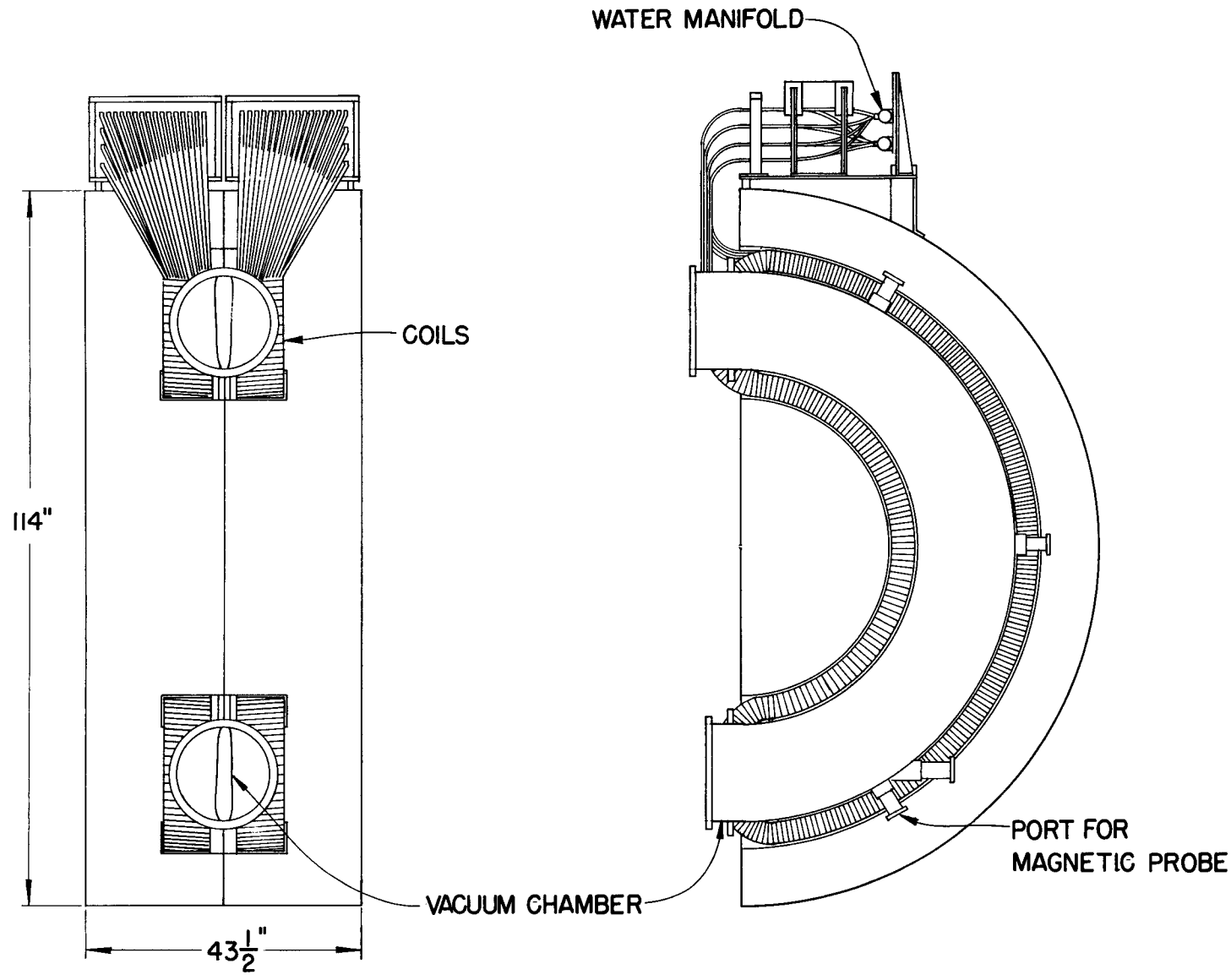

FIG. 2.——Details of the magnetic spectrometer.

5e-35

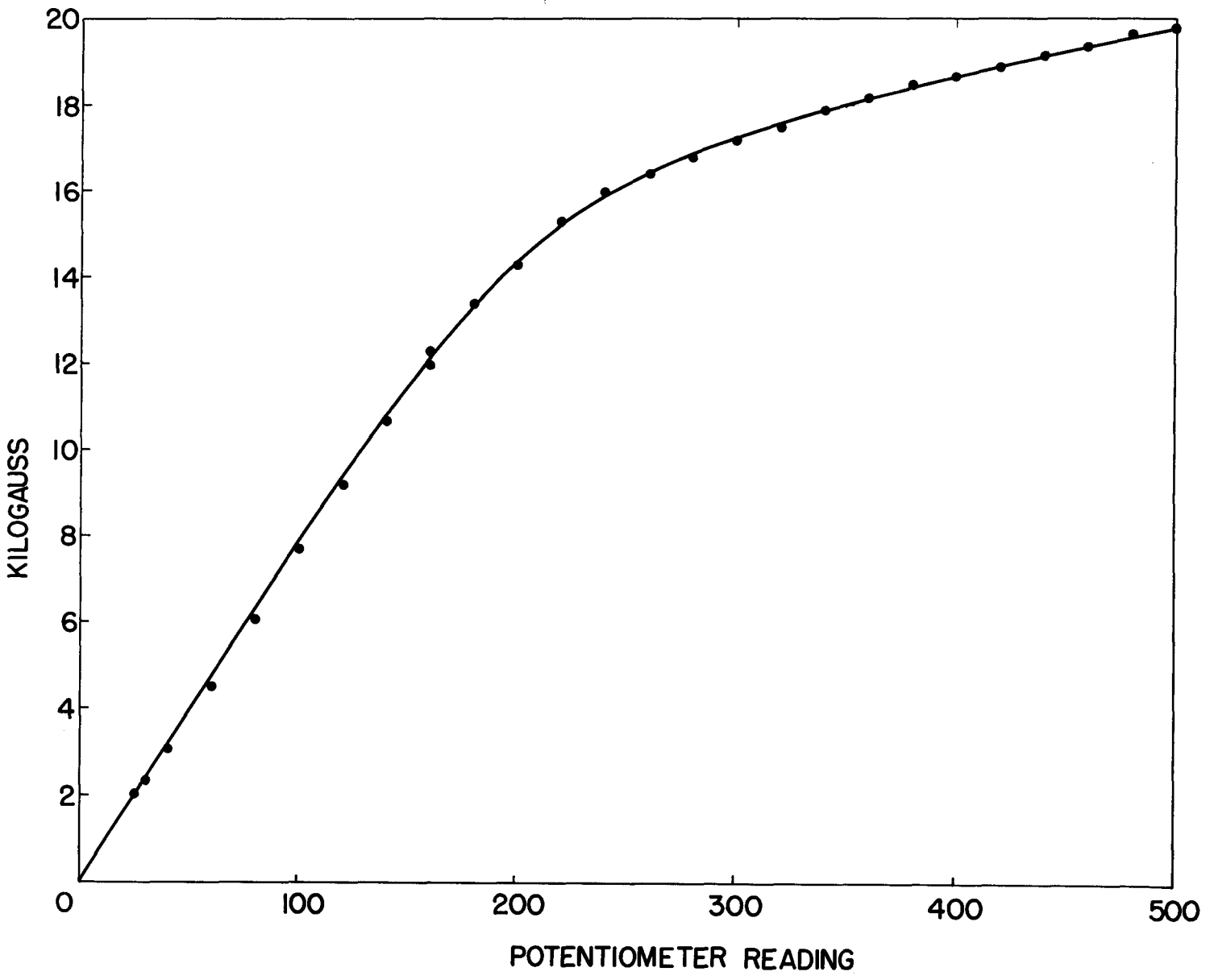

FIG. 3.——A typical radial plot of magnetic field in the median plane vs current in the magnetizing coils.

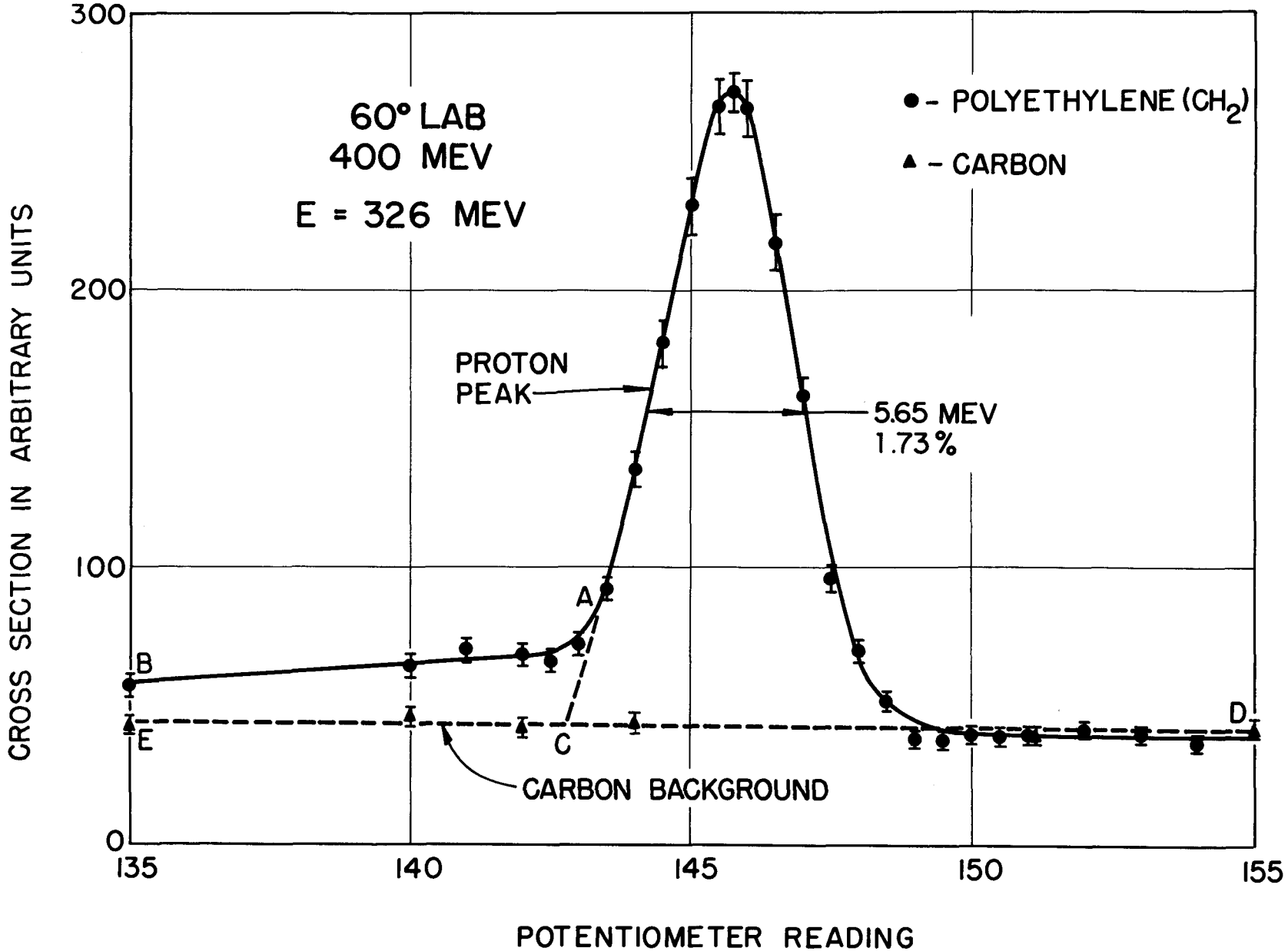

FIG. 4.——An elastic profile at 60° and 400 Mev, showing the data taken with polyethylene and the background points due to carbon. The potentiometer reading is proportional to the magnet current, which, in this region of the spectrometer characteristic, is proportional to energy.

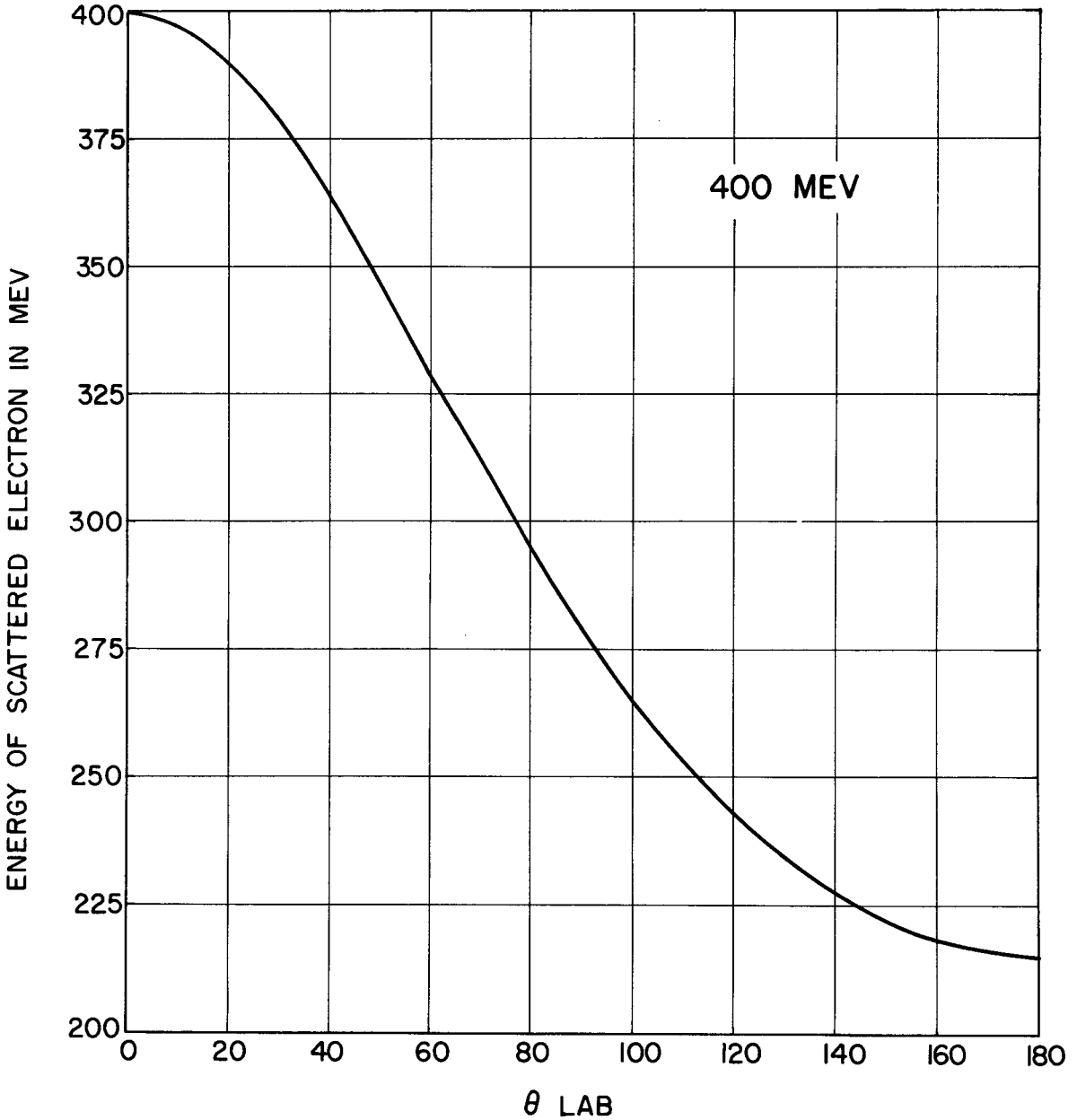

FIG. 5.——A theoretical curve found by employing relativistic kinematics of the two-body, electron-proton collision, showing the energy of the scattered electron vs angle of scattering in the laboratory frame.

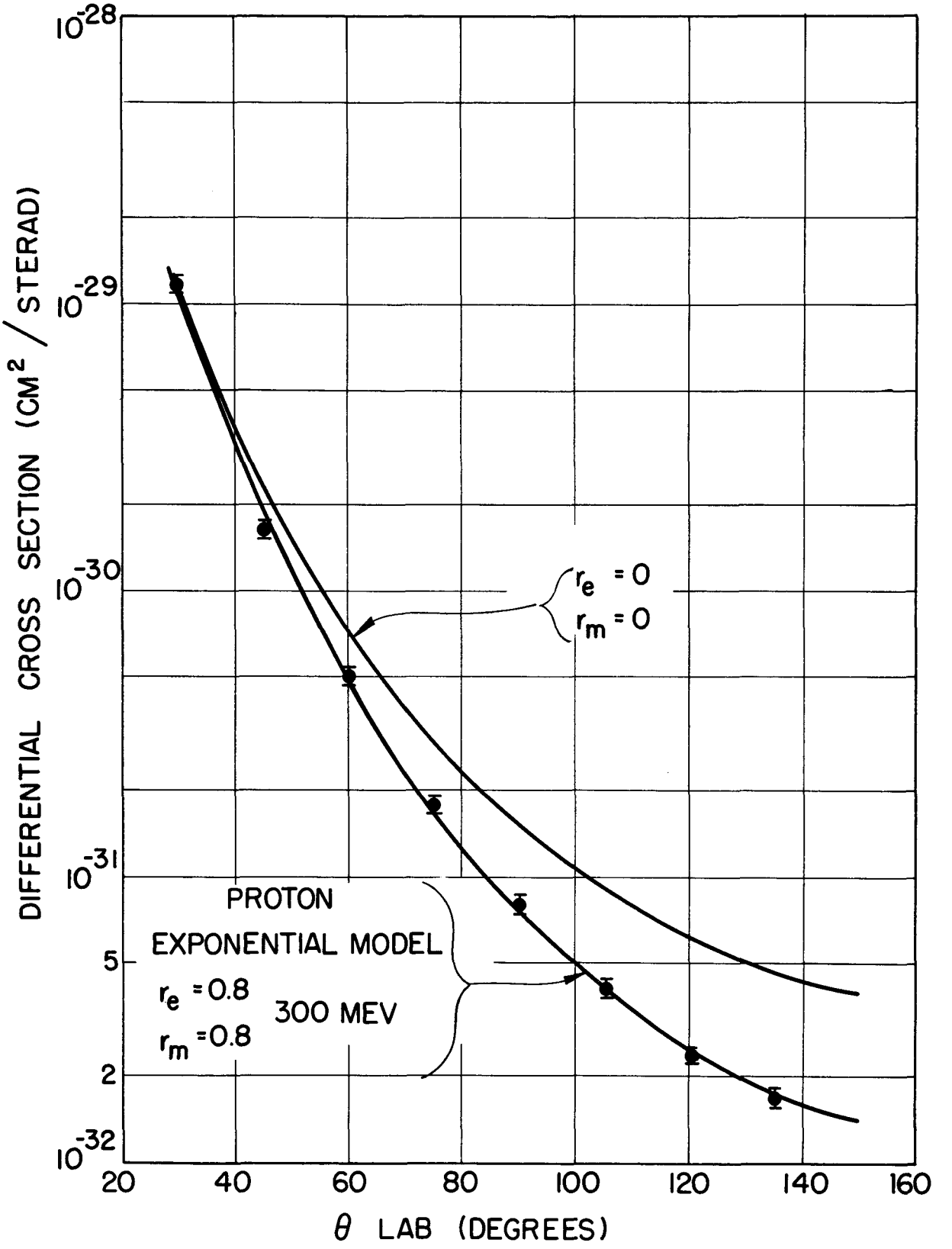

FIG. 6.——The experimental points showing the relative angular data taken at 300 Mev. The point-charge curve ($r_e = 0$, $r_m = 0$) is shown above. The solid line running through the points is the theoretical curve obtained from Eq. (3) for an exponential proton with rms radii $r_e = 0.8$ fermi and $f_m = 0.8$ fermi and represents a best fit to the data for an exponential model.

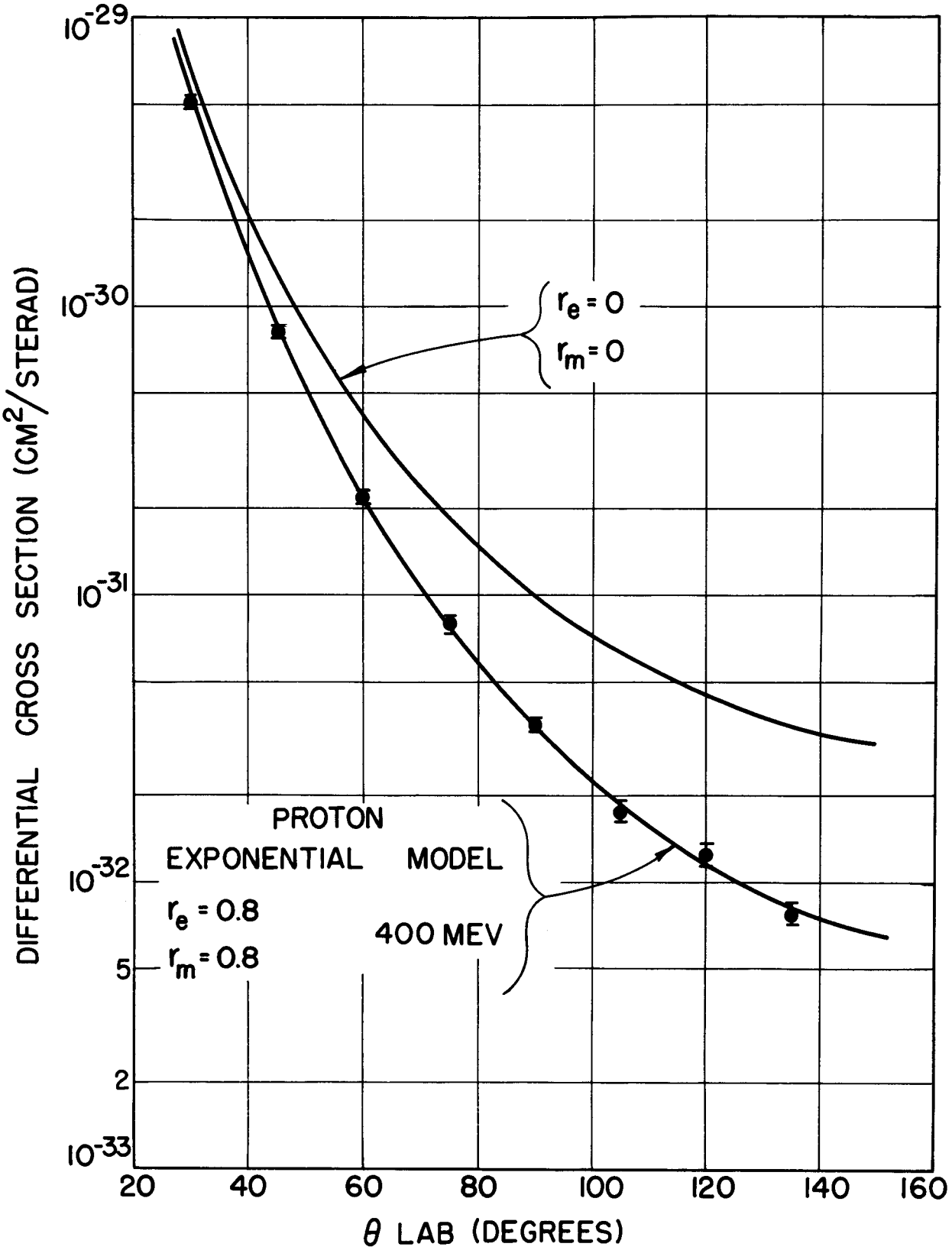

FIG. 7.——The experimental points at 400 Mev. Theoretical calculations are similar to those referred to in the legend of Fig. 6.

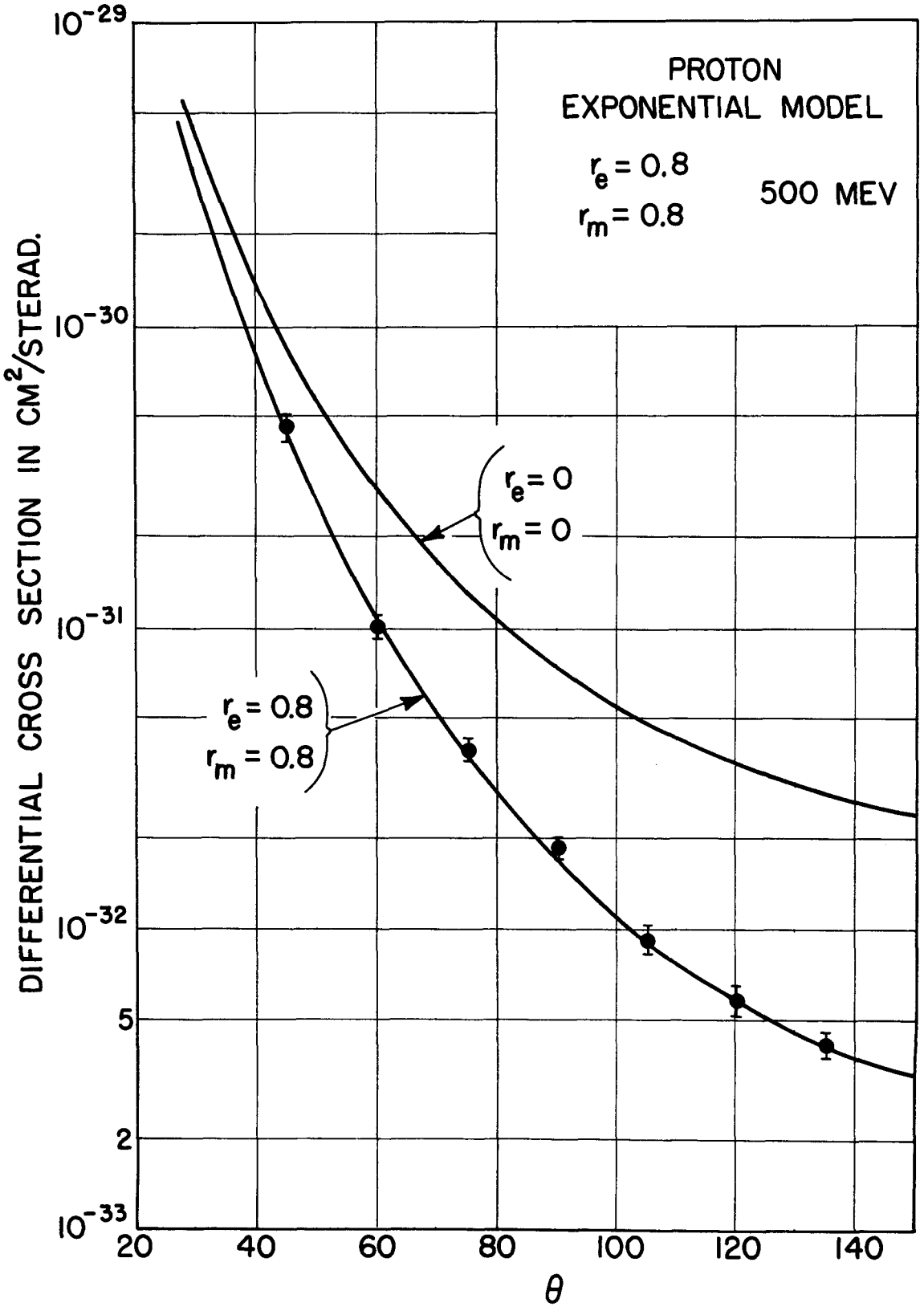

FIG. 8.——The experimental points at 500 Mev. The theoretical calculations are similar to those referred to in the legend of Fig. 6.

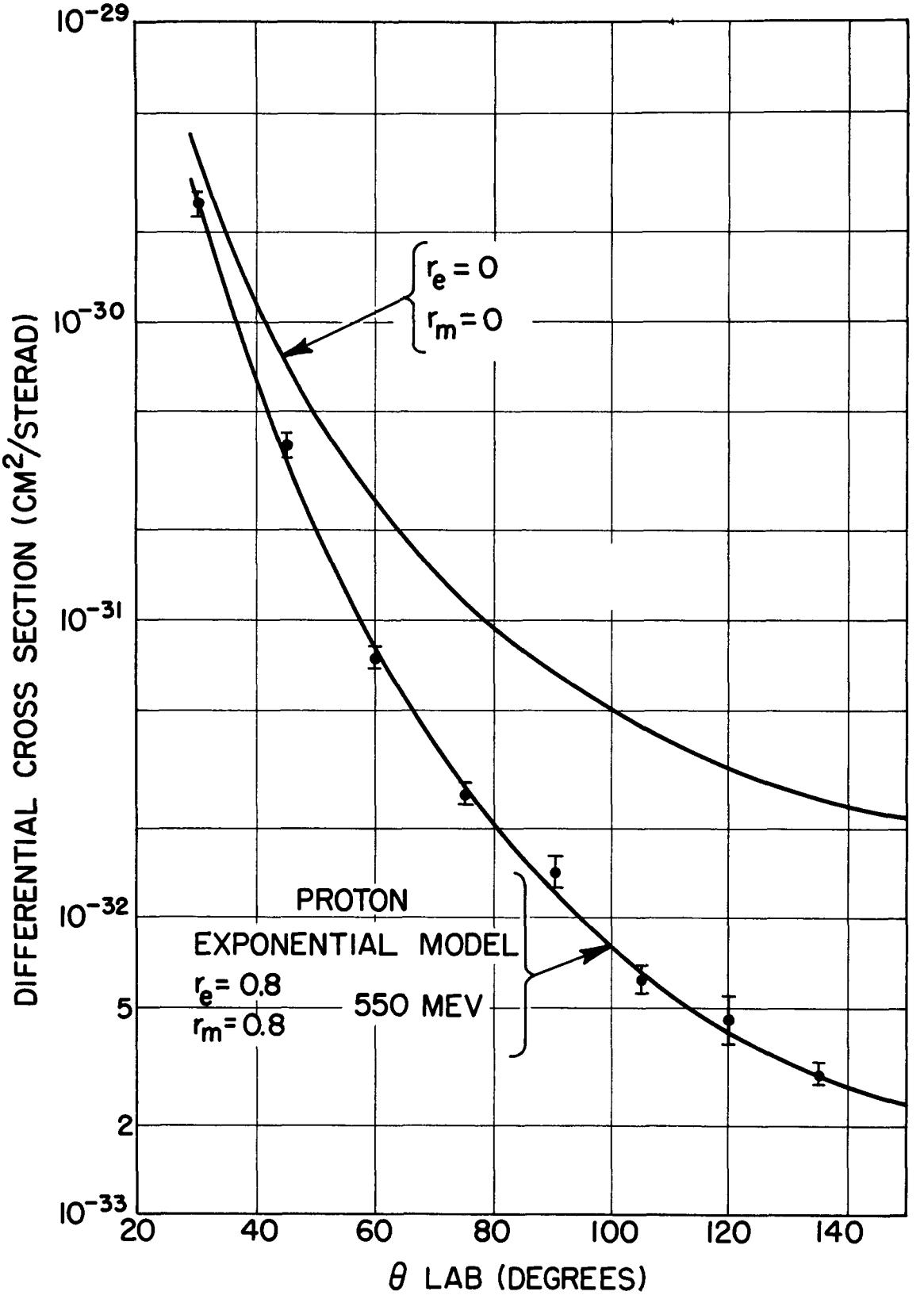

FIG. 9.——The experimental points at 550 Mev. The theoretical calculations are similar to those referred to in the legend of Fig. 6.

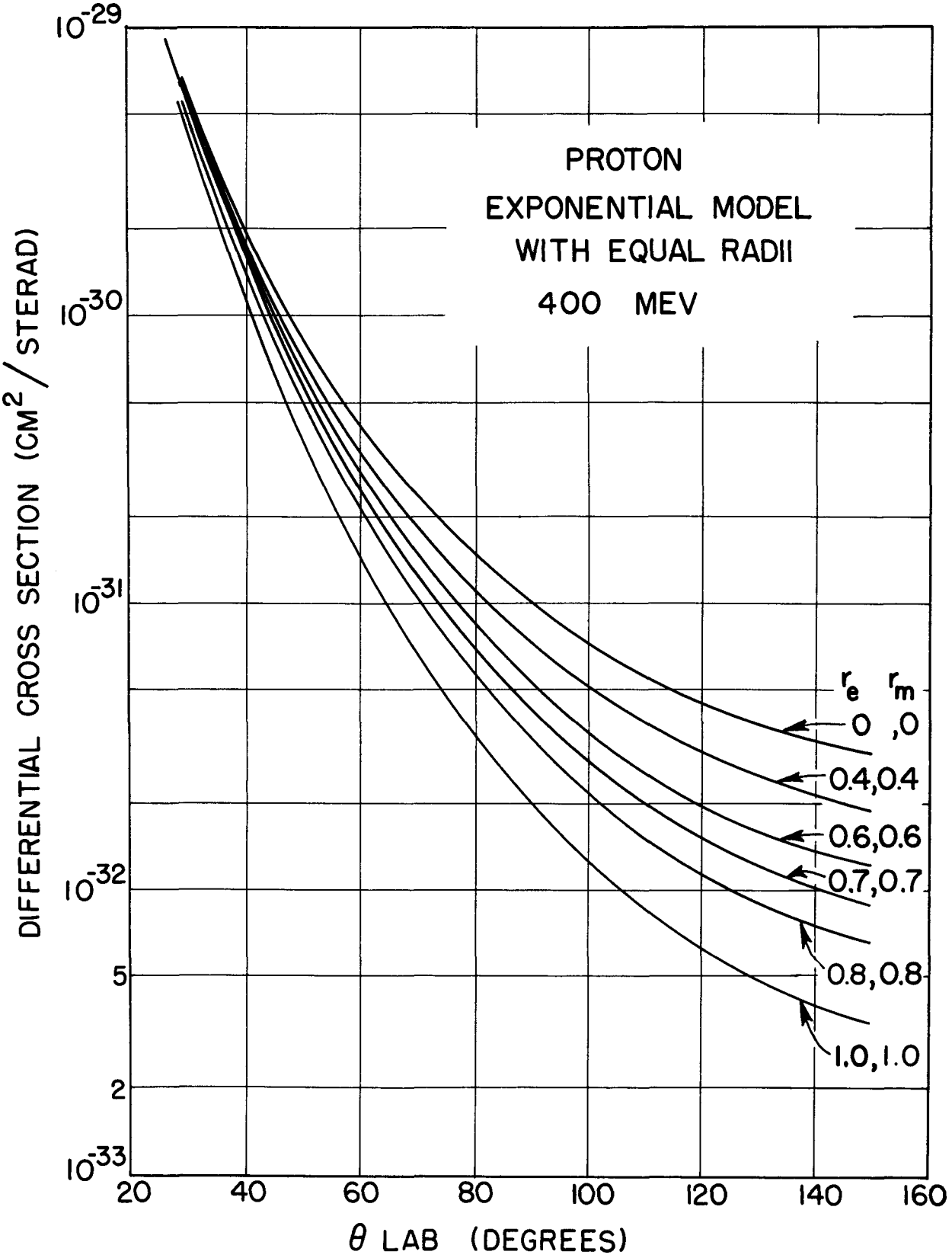

FIG. 10.——Shown are the point-charge curve $r_e = 0$, $r_m = 0$ and various theoretical curves for an exponential proton with equal radii, such as 0.4,0.4 up to 1.0,1.0. These curves were obtained from Eq. (3) and the form factors F_1, F_2 appropriate to an exponential model with the stated rms radii.

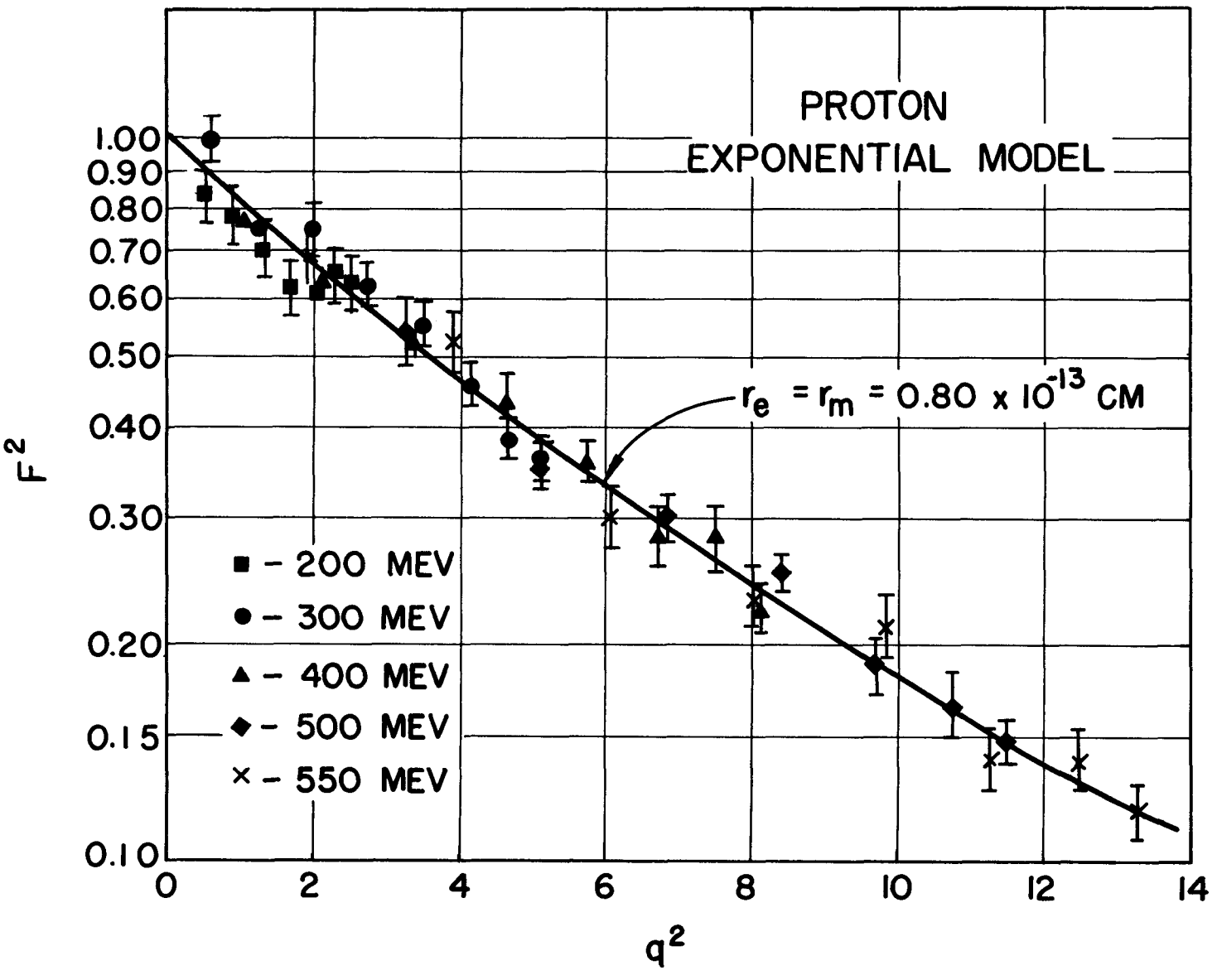

FIG. 11.——Summary of the comparison between the exponential model with equal radii (0.8 fermi) and the experimental points. The square of the form factor is plotted against q^2 where q is given by Eq. (3).

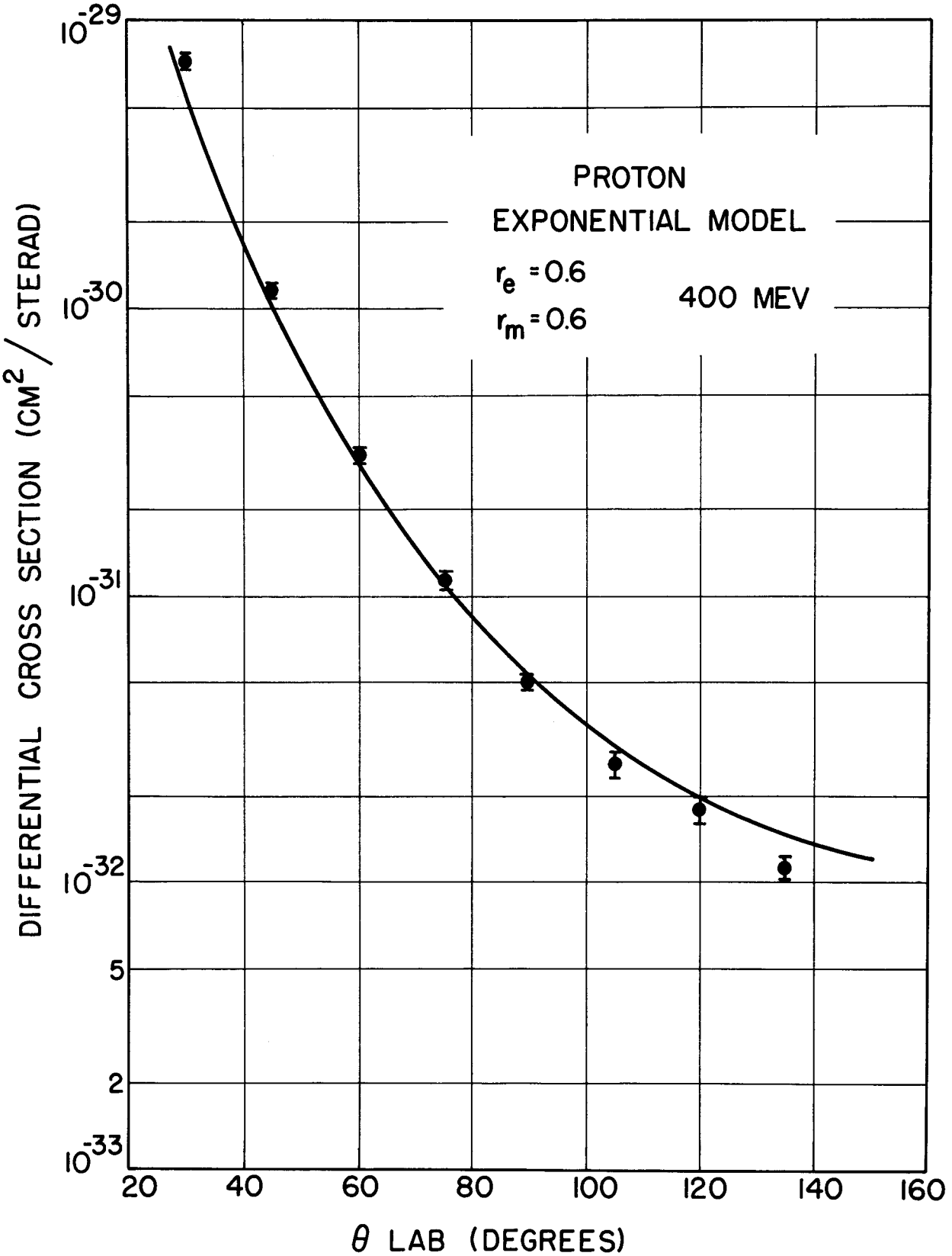

FIG. 12.——The comparison of the experimental points with an exponential model with radii equal to 0.6 fermi. This is an example of a model which does not fit and shows the tolerance of the fit allowed by experiment.

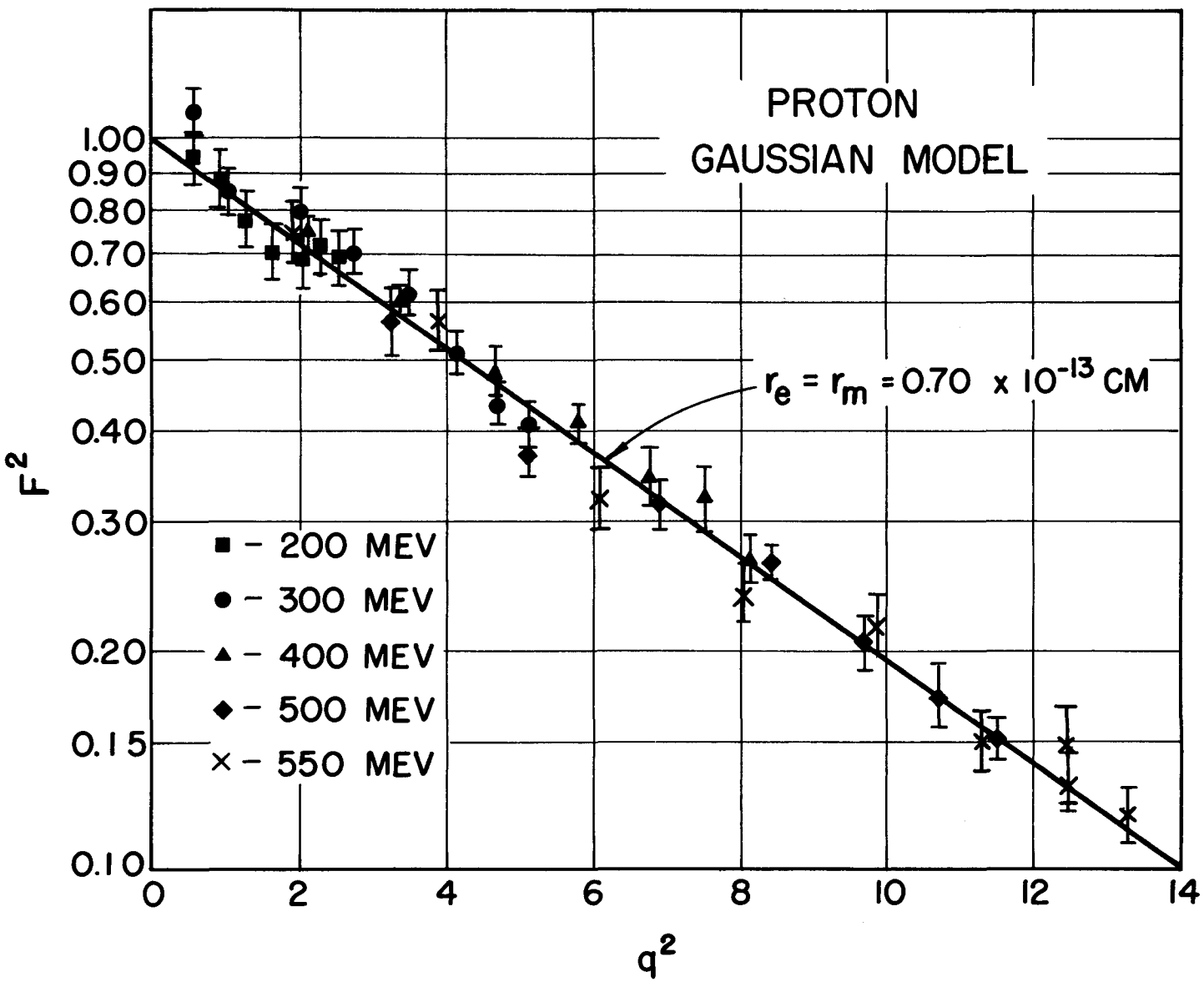

FIG. 13.——Summary of a comparison between the Gaussian model with equal radii (0.7 fermi) and the experimental points. In this case the theoretical plot is a straight line.

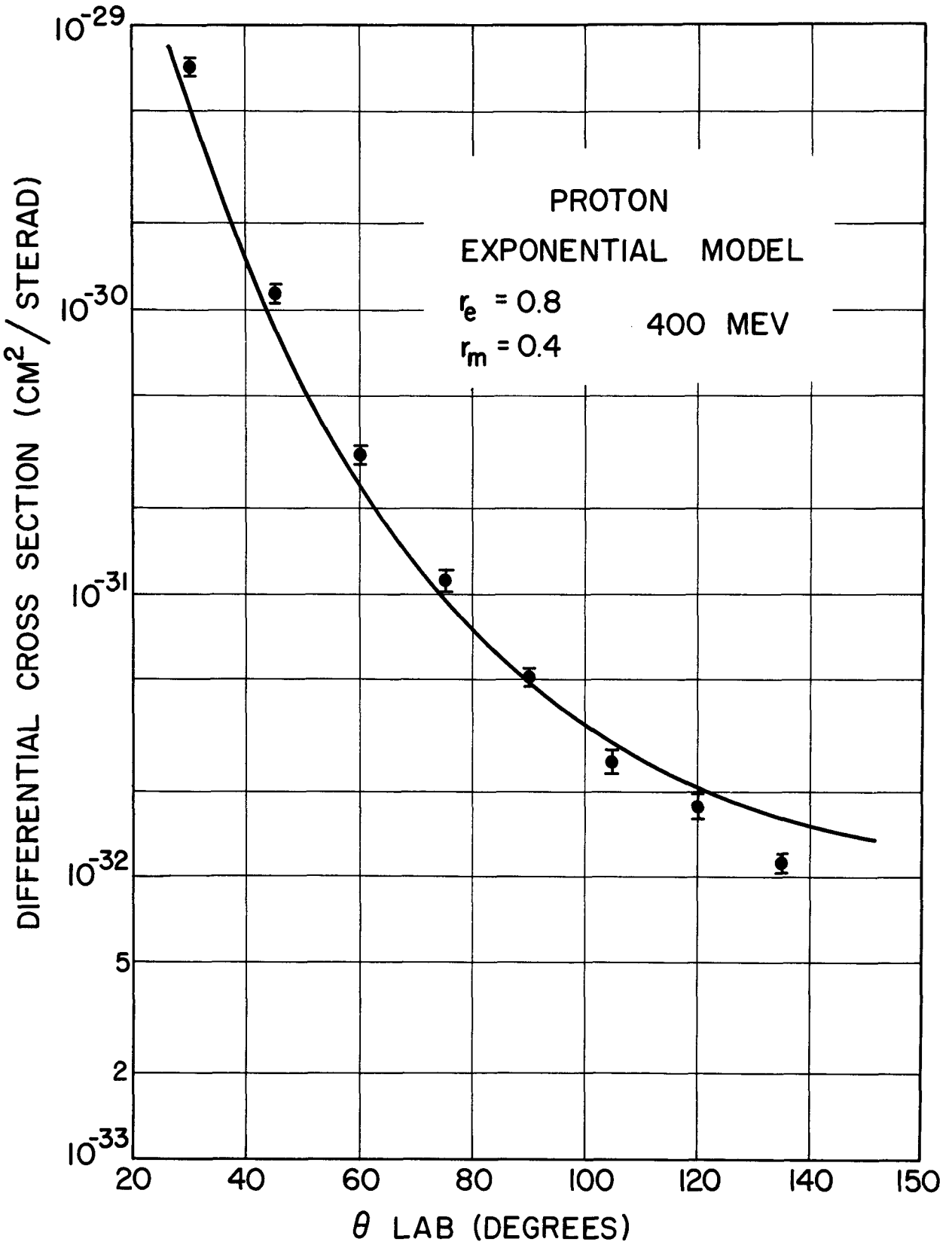

FIG. 14.——Attempt to fit the data at 400 with a small magnetic-moment distribution.

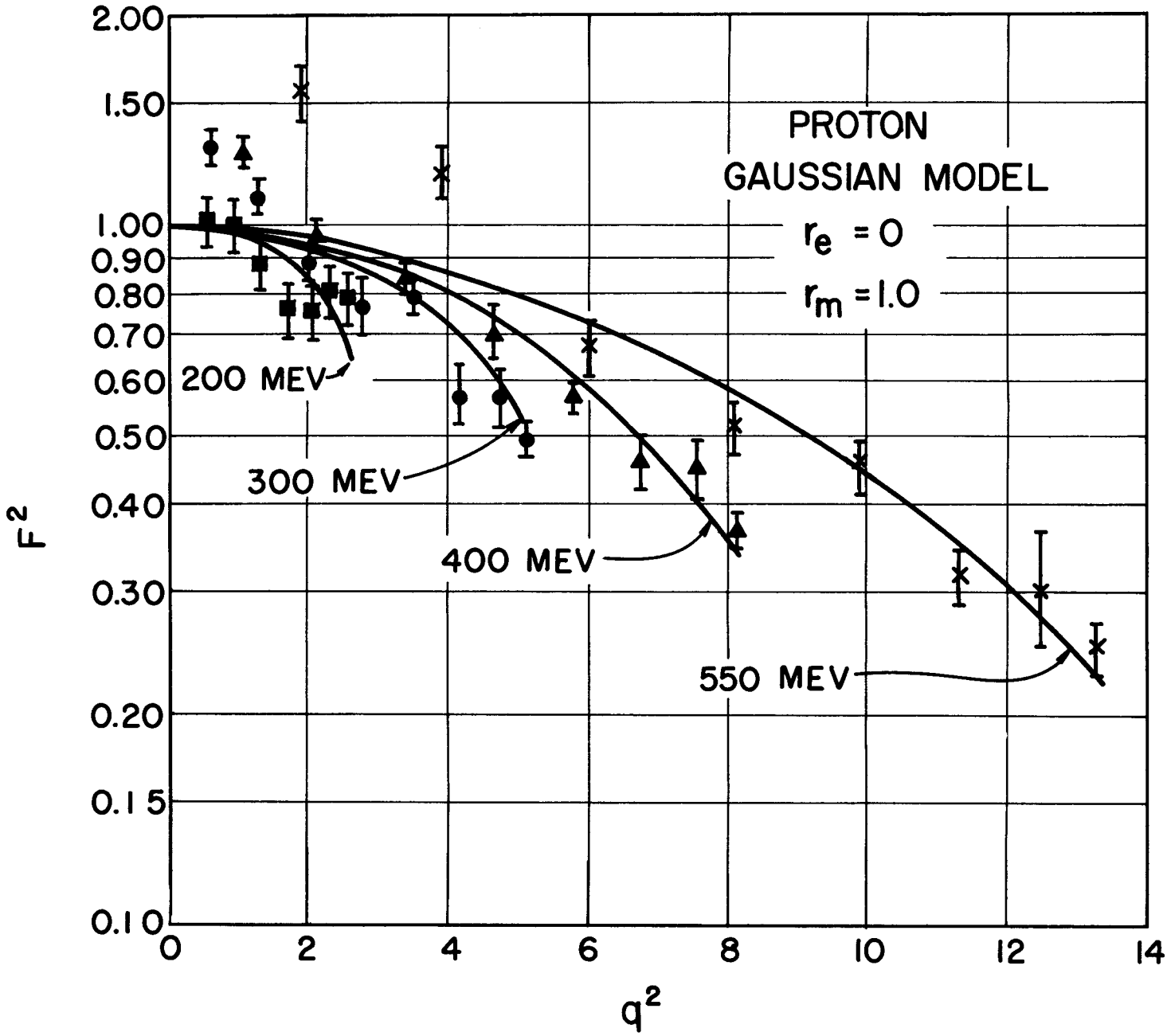

FIG. 15.——An attempt to fit the data at all energies with a Gaussian proton having $r_e = 0$, $r_m = 1.0$. The fit is not good and this model can be excluded. Separate curves are required for different energies.

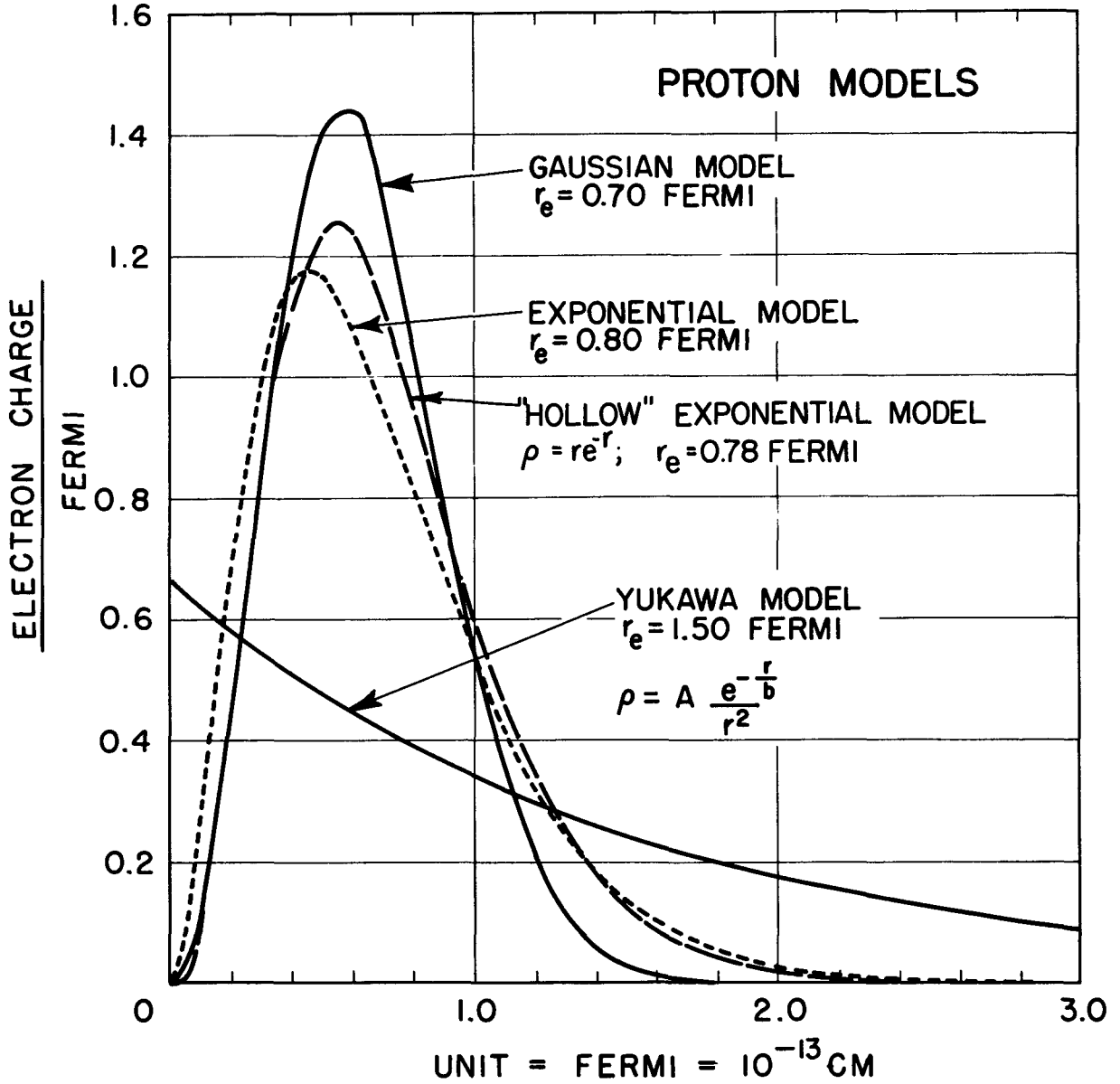

FIG. 16.——Shown in the figure are three charge distributions (Gaussian, exponential, and hollow exponential) which fit the data at all energies and angles. The hollow exponential is the best overall fit of the three. In the figure the ordinate is $4\pi r^2\rho$, a quantity proportional to the amount of charge in a shell at radius r. The Yukawa and uniform models are examples of charge distributions which will not fit the data. In all cases r_e refers to the best value of the rms radius of the charge distribution. r_m is taken equal to r_e.